Z. Phys. D 30, 1–12 (1994)

ZEITSCHRIFT
FÜR PHYSIK D

Picosecond photoelectron studies of cluster dynamics

Invited Progress Report

J.A. Syage

The Aerospace Corporation, P.O. Box 92957/M5-754, Los Angeles, CA 90009, USA

Received: 25 October 1993

Abstract. Time-resolved photoelectron spectroscopy is proving to be a versatile tool for investigating dynamical properties of molecules and clusters. In this account we review our recent work involving studies of cluster reactivity by photoelectron spectroscopy. Two topics are discussed. The first, involves measurements of the rate of solvent reorganization and the magnitude of the solvent reorganization energy (i.e., the solute-solvent interaction). The solvent rearrangement is induced by an excited-state proton transfer in phenol-ammonia clusters. These studies are motivated by the opportunity to probe condensed-phase solvation effects on a molecular level in clusters. The second topic describes how the chemical properties of small clusters (e.g., dimers) provides detailed information regarding the collision complexes of bimolecular gas-phase reactions. We show an example of how the combination of photoelectron spectroscopy and ion fragmentation mass spectrometry can be used to determine barrier heights for bimolecular reactions.

PACS: 34.30; 36.40; 82.30.N

1. Introduction

Clusters are a popular means of studying properties of the bulk on an atomic or molecular level and for understanding departures from bulk-phase behavior as the system size approaches the single-molecule gas-phase limit. Our work centers on the study of chemical reactivity in clusters using time-domain techniques [1–6]. This field of endeavor has been growing rapidly lately [7–12]. In a typical experiment, a molecular beam of clusters is photoexcited to a reactive state by a pump pulse, and the relative reactant and product yields are measured by a variably-delayed probe pulse using multiphoton ionization. Most of our experiments use a time-of-flight mass spectrometer in order to measure dynamics as a function of cluster size [1–4]. More recently, we have applied the technique of time-resolved photoelectron spectroscopy (TR/PES) to the measure of dynamical properties in clusters [5, 6, 13].

The advantage of TR/PES for studying dynamics in molecules is that a photoelectron spectrum measures the Franck-Condon transitions from an initial or intermediate state, and is therefore sensitive to changes in these states [14]. Knee and coworkers made measurements of intramolecular vibrational relaxation (IVR) of fluorene and observed quantum beats in the photoelectron time-dependence [15]. Riley and coworkers recorded photoelectron spectra from electronically excited alkyl anilines that broadened as a function of time, which they attributed to IVR [16]. Other examples of TR/PES have been reported by the groups of Kimura [17], Gerber [18], Weber [19], and ourselves [6, 14]. Applications of TR/PES to cluster dynamics include studies of IVR and vibrational predissociation in aniline-CH_4 by Knee and coworkers [20], coherent excitation in Na_2 and Na_3 by Gerber and coworkers [18], and solvent reorganization in phenol-$(NH_3)_n$ by our group [6].

In this article we review our recent studies of cluster dynamics with particular emphasis on the information gained by PES. We will focus on two case studies involving proton transfer from phenol to ammonia solvent in clusters. In the first case, we exploit clusters as a molecular-level model of condensed-phase chemistry. PES is used to measure the time dependence of the geometric rearrangement of the solvent following a proton transfer reaction. In the second study, we utilize small clusters (e.g., dimers) as a model for the collision complex in gas-phase bimolecular reactions. We show how details of the barrier region are obtained by a combination of ion photofragmentation mass spectrometry and photoelectron spectroscopy.

2. Experimental details

2.1. Paraboloidal electrostatic reflector (PER) *photoelectron spectrometer*

Conventional time-of-flight (TOF) photoelectron spectrometers collect very small solid angles of electrons. While this arrangement is acceptable for most applica-

tions, it can be inadequate for many experiments that use low laser powers (e.g., picosecond pulses), low densities of material (e.g., a specific cluster size), multiphoton excitation, or excitation through a dissociative state. Since our work often involves any one of these conditions, we opted to construct a spectrometer that collects a large solid angle of electrons while maintaining the integrity of a TOF measurement for determining electron energies. This is achieved by employing a paraboloidal electrostatic reflector (PER) for reflecting and collimating electrons [13]. Our PER is based on the design by Trevor, Van Woerkom, and Freeman and consists of two concentric slightly separated paraboloidally shaped grids that are biased at different potentials to create a reflecting field for electrons [21]. An alternative method for obtaining high collection efficiency in a time-of-flight configuration is to use magnetic field collimation (e.g., a magnetic-bottle spectrometer) [22]. However, compared to the PER approach, the magnetic bottle does not preserve the angular information for ionization, subjects the excitation volume to high magnetic fields, and involves a relatively complex design. Zero-kinetic-energy/pulsed-field ionization (ZEKE/PFI) photoelectron spectroscopy offers high sensitivity and high resolution, but is a double-resonance technique that requires two tunable laser sources, one to excite to an intermediate state and the other to excite to an ion vibronic threshold to give near zero-kinetic-energy electrons (or actually field ionized very high n Rydberg states) [23]. Furthermore, ZEKE detects one ion state at a time, as opposed to the TOF method, which records an entire ion spectrum. ZEKE, however, provides far superior energy resolution.

A schematic of the molecular beam photoelectron spectrometer is illustrated in Fig. 1. The apparatus consists of a source chamber and a photoelectron chamber. Optical ports allow the laser beam to pass into the source chamber immediately in front of the pulsed valve for mass spectrometric studies or into the experimental chamber through the paraboloidal mirror assembly for photoelectron spectroscopy studies [13]. The apparatus is equipped with a temperature-controlled pulsed valve. Typical operating conditions are 10–25-psi Ar backing pressure, 500–750-μ nozzle aperture, 200–300-μs pulse width, 4-cm nozzle-skimmer distance, and 1-mm-diam skimmer. Typical chamber pressures at 10-Hz operation are $5\text{–}10\times10^{-6}$ Torr and $5\text{–}20\times10^{-8}$ Torr for the source and photoelectron chambers, rising from base pressures of 4×10^{-7} Torr and 3×10^{-8} Torr, respectively.

The details of the PER/PES components are shown in the insert to Fig. 1. The PER consists of two paraboloidal grid forms, separated by 2–3 mm at the apex, and biased to create a -5 V reflecting field for electrons. The intersection of the laser and molecular beams takes place at the focal point of the PER. All reflected electrons are collimated and travel the same path length toward the detector. The drift tube is 1 m long. A one to two order of magnitude enhancement is observed for reflected electrons versus direct electrons. The direct electrons are currently unblocked and arrive at the detector about 2% sooner than reflected electrons of the same energy. The volume encompassed by the inner paraboloid and flat grid is maintained at zero field. Electrons can be accelerated into the drift tube to enhance detection efficiency, which is particularly useful for low energy electrons.

An einsel-lens assembly at the end of the 9-cm diam drift tube is used to focus the electrons onto a 4-cm diam detector. The PER and drift tube are shielded from stray magnetic fields by two layers of μ-metal. The relatively strong signal levels permit the use of analog detection.

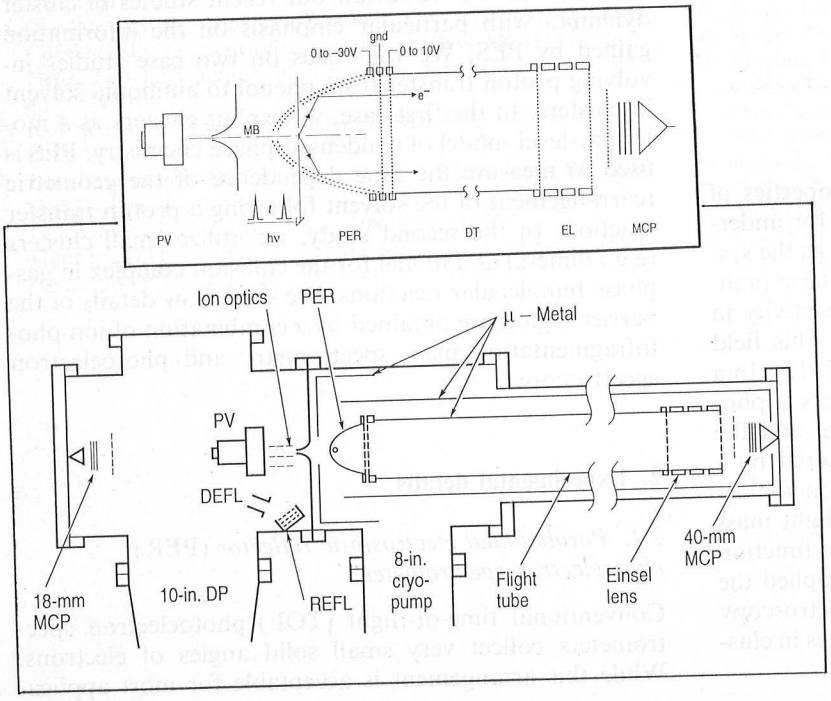

Fig. 1. Experimental schematic of the molecular beam photoelectron spectrometer and an enlargement of the PER section. Terms are defined as follows: DEFL – deflector plates; DP – diffusion pump; DT – drift tube; EL – einsel lens; $h\nu$ – pump-probe pulses of delay time t; MCP – microchannel plate detector; PER – paraboloidal electrostatic reflector; PV – pulsed valve; REFL – reflecting grids

Energy-resolved photoelectron spectra are recorded using a digital storage oscilloscope (350-MHz, 400-Mhz sampling rate) and built-in signal averaging. Time-resolved spectra are recorded using a gated integrator set to collect signal from specific energy bands in the TOF photoelectron spectra. The instrument routinely achieves resolution of $\Delta E/E = 0.02$, but can be improved to 0.005 (to a limit of $\Delta E = 10$ meV). A complete description of the apparatus is given elsewhere [13].

The cluster samples are prepared by a variety of procedures. Solid compounds, such as phenol, were placed in a sample holder in the pulsed valve and heated to 40–60 °C. For ammonia solvation, a 2-liter high-pressure cylinder was made up containing 1–10% ammonia in helium or argon. Water and methanol solvation was achieved by flowing helium through a bubbler containing either of these solvents.

2.2. Excitation and detection

In this work, chemistry is initiated by a photoexcitation pulse and the evolution of cluster properties are interrogated at later times by various probe excitation and detection techniques. A number of possible choices for the pump and probe pulses are available from the Nd:YAG harmonics and the dye laser (the latter employs the usual wavelength extension capabilities, e.g., doubling, mixing, Raman shifting). Two frequently used pump-probe arrangements are (1) 266 nm as the pump and 532 nm (or 355 nm) as the probe and (2) tunable UV output from the dye laser as the pump and 355 nm as the probe. We employ other combinations on occasion for both cluster and non-cluster work (i.e., 266 + Vis, UV + 532, UV + Vis). All chemistry discussed here was initiated using single-photon excitation in the UV. Probe ionization was achieved using single-photon and multiphoton excitation. In some instances, it was advantageous to use high ionization energy to dissociate the resulting cluster ions. This is the case when reactant and product clusters are of the same mass (e.g., in proton transfer) and not easily distinguishable by mass spectrometry unless they have different propensities for dissociating as ions.

3. Background on excited-state proton transfer in clusters

Cheshnovsky and Leutwyler were the first to study excited-state proton transfer (ESPT) in clusters by investigating the system 1-naphthal-$(NH_3)_n$ [24]. These studies were followed by other steady-state experiments and more recently by time-resolved methods. Aromatic alcohols such as phenol and naphthol are known to be more acidic in their S_1 state than in S_0 (the so-called pH jump) [25]. These reactions have been studied extensively in the condensed phase including several time-resolved experiments [25–27]. We have carried out mass-resolved picosecond measurements of the phenol (PhOH) ESPT reaction [2–4]. The proton transfer, represented by

$$PhOH^* B_n \xrightarrow[k]{} PhO^{*-} H^+ B_n$$

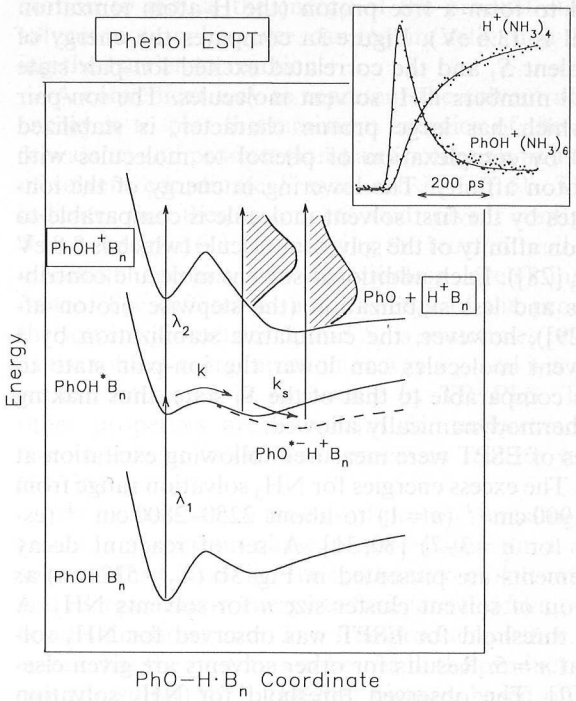

Fig. 2. Energy diagram for $PhOH(NH_3)_n$ consistent with a cluster size of $n \sim 5$. The pump and probe pulses are denoted as λ_1 and λ_2, and the ESPT and solvent reorganization rate constants are given by k and k_s, respectively. The expected photoelectron band shapes resulting from these processes are also shown. The ion signals for reactant and product are given in the insert and show matching kinetics. A lower n value for the product is plotted to reflect the loss of two NH_3 that evaporate on average in the dissociative ionization step [2, 3]

corresponds to a conversion from the locally excited S_1 state of the phenol acid to an excited ion-pair state (B_n refers to the solvent cluster consisting of n molecules of base B). A qualitative picture of the cluster potential energy curves for ground, excited, and ionic states is given in Fig. 2 along with the picosecond pump-probe excitation/detection scheme used to measure the chemical rates. Figure 2 also shows representative ion energy distributions, measurable by photoelectron spectroscopy. Reactant and product are distinguishable in our experiments by mass spectrometry because they fragment differently upon ionization. Ionization of reactant clusters $PhOH^* \cdots B_n$ produces cluster ions $PhOH^+ \cdots B_n$ on the inner potential well where the O—H coordinate is strongly bound. Conversely, ionization of the product ion-pairs $PhO^{*-} \cdots H^+ B_n$ produces cluster ions $PhO \cdots H^+ B_n$ on the outer well where facile dissociation occurs to give $H^+ B_n$. The observed reactant and product signals show matching kinetics, which is important for establishing that the observed response is a proton transfer reaction.

The ion-pair or proton-transfer states in clusters (or condensed phase) are associated with charge transfer states in gas-phase molecules. Charge-transfer states generally occur at high energy. In phenol, the relevant states are expected to lie at very high energy relative to the covalent S_0 and S_1 states because of the large energy

required to form a free proton (the H atom ionization potential is 13.6 eV). Figure 3a compares the energy of the covalent S_1 and the correlated excited ion-pair state for small numbers NH_3 solvent molecules. The ion-pair state, which has large proton character, is stabilized strongly by complexation of phenol to molecules with high proton affinity. The lowering in energy of the ion-pair states by the first solvent molecule is comparable to the proton affinity of the solvent molecule (which is 8.8 eV for NH_3 [28]). Each additional solvent molecule contributes less and less stabilization (the stepwise proton affinity [29]), however, the cumulative stabilization by a few solvent molecules can lower the ion-pair state to energies comparable to that of the S_1 state, thus making ESPT thermodynamically allowed.

Rates of ESPT were measured following excitation at 266 nm. The excess energies for NH_3 solvation range from about 1900 cm^{-1} ($n=1$) to about 2250–2800 cm^{-1} (estimated for $n=3$–7) [30, 31]. A set of reactant decay measurements are presented in Fig. 3b ($\lambda_2=532$ nm) as a function of solvent cluster size n for solvents NH_3. A distinct threshold for ESPT was observed for NH_3 solvation at $n=5$. Results for other solvents are given elsewhere [2]. The observed threshold for NH_3 solvation agrees closely with the simple potential model in Fig. 3a, lending support to the notion that solvation of high energy ion-pair states is the mechanism of acid-base chemistry in condensed phase.

4. Solvent dynamics in clusters

The energy diagram and measured ESPT rates in Fig. 3 attest to the strong interaction that solvent molecules exert on chemistry. The simple discussion above treats these interactions as static, which we define as some fixed energy stabilization for some fixed solvent geometry (implicitly assumed to be the equilibrium geometry). Chemistry also depends on dynamical properties of the solvent in a number of ways. How much do the reactant and product energy levels fluctuate due to fluctuations or vibrations in the solvent? Does the solvent reorganize efficiently during and after reaction? How important are solvent dynamics in promoting reactions? Is the range of solvent motion sufficiently large to find the lowest energy configuration for intermediates or products (or can they lie outside the Franck-Condon region)? Certainly the list of question does not end here.

4.1. *Tunneling and barrier properties for* ESPT

The measured rate of ESPT for deuterated phenol/ammonia clusters is over an order of magnitude slower than for protiated clusters strongly indicating that tunneling is involved [32]. The same conclusion was reached by Hineman, Bruker, Kelley, and Berstein (HBKB) for 1-naphthol/ammonia clusters [11]. What is still not understand is the mechanism of tunneling in clusters and whether solvent motion is important. In this regard, TR/PES provides valuable information regarding solvent reorganization energy, which is an important property for solvent-activated tunneling (i.e., dynamic solvent effect) [33–36].

We call attention to three important coordinates for proton tunneling, the O—H coordinate, which is the reaction coordinate, the O···N coordinate, which affects the barrier properties, and the solvent coordinate, S, which affects the relative energies of reactant and product [32]. The O—H potential for fixed O···N distance is represented in Fig. 4. For a splitting of about 1 eV [33], we represent the barrier by a parabolic function with an equilibrium barrier height and width of $U_0=0.4$ eV and $a_0=0.30$ Å, respectively [32]. The relative well depths depend on the static properties (i.e., number and type of solvent molecules) and dynamic properties (solvent geometry and fluctuations). The symmetric potential shown in Fig. 4 is assumed to correspond to a specific solvent configuration that we call $S^{\ddagger}$. This configuration will most likely be different from the equilibrium solvent geometries of the reactant covalent and product ion-pair states, S_r and S_p, respectively. Schematic representations of the The O—H potential for S_r and S_p are given in Fig. 5a. This picture is important because it implies that an exothermic reaction occurs only if there is solvent

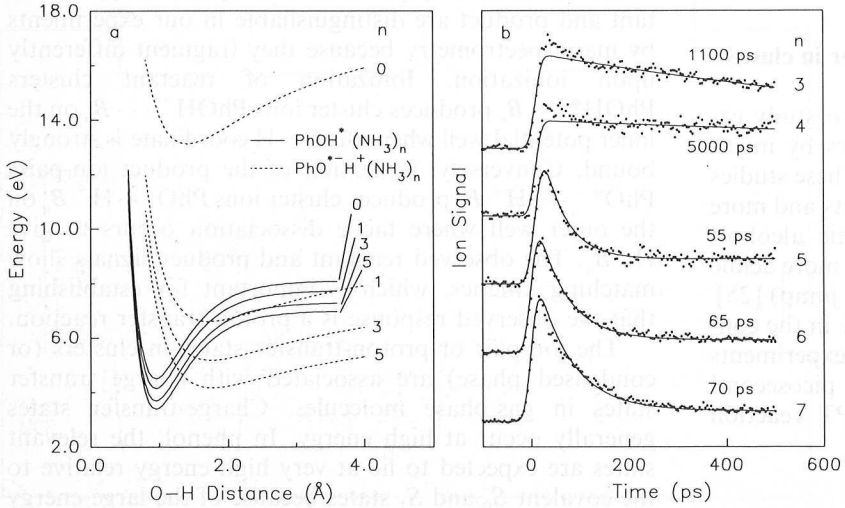

Fig. 3. a Approximate PhOH $(NH_3)_n$ cluster potential energy curves for the reactive PhO—H coordinate. These curves assume an equilibrium O···N bound distance (approximately 1.8 Å and 1.0 Å for the neutral and ion-pair states, respectively). **b** Observed lifetimes of reactant PhOH* $(NH_3)_n$ (as measured by $PhOH^+$ $(NH_3)_n$ detection). The calculated curves are described elsewhere [2]

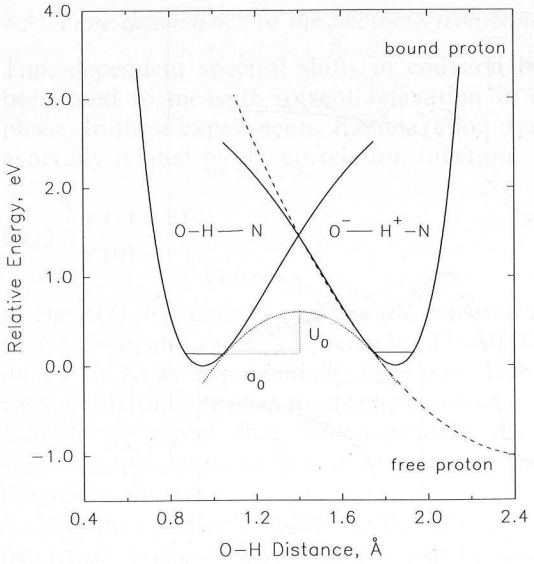

Fig. 4. Barrier to ESPT arising from the crossing of a covalent and ion-pair potential for PhOH*$(NH_3)_5$. A parabolic function, used for the tunneling calculations, is fitted to the crossing region; a_0 and U_0 are the barrier halfwidth and height measured from the vibrationless level of O—H. The free proton potential is described in the text

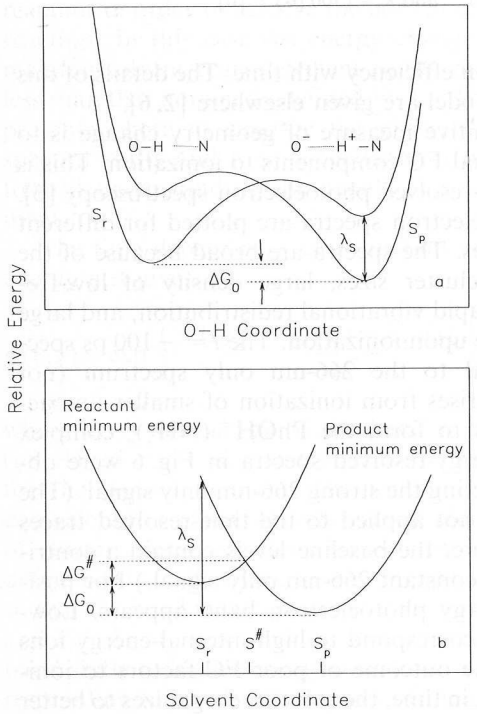

Fig. 5. a Schematic representation of the potential energy along the O—H coordinate for fixed solvent configurations S_r and S_p. **b** Reactant and product minimum energy as a function of solvent coordinate S. $\Delta G^{\ddagger}$ is the free energy of activation for achieving resonance between the reactant and product minimum (vibrationless) energy. ΔG_0 is the free energy of reaction for an equilibrating solvent. λ_S is the solvent reorganization energy

motion to reduce the energy of the product state. This solvent motion, however, can require activation thus raising the barrier to reaction.

A convenient way to represent the solvent activation energy is to plot the minimum energies of the reactant (covalent) and product (ion-pair) potentials as a function of solvent coordinate S as shown in Fig. 5b. This view indicates that there is an activated solvent configuration $S^{\ddagger}$ at energy $\Delta G^{\ddagger}$ for bringing the reactant and product minimum energies (or vibrationless levels) into resonance. The difference in the energy of the product for the solvent geometries S_r and S_p is sometimes referred to as the solvent reorganization energy λ_S, and is a quantity we are interested in measuring by TR/PES. This and other properties are important for understanding the role of solvent in chemical processes such as tunneling [34–36].

We examined two models of proton tunneling in clusters; (1) a solution-phase picture based on a dynamic solvent effect involving the mechanism of solvent motion and reorganization energy to facilitate tunneling (bound-bond transition) and (2) a free-product picture that assumes that the proton is unbound in the product (bound-free transition) [32]. The first picture, based on the potential model in Fig. 5 for solvent activation, assumes that proton tunneling occurs only when the solvent attains a configuration $S^{\ddagger}$, for which the reactant and product statesare degenerate [34–36]. The second picture, advanced by HBKB for 1-naphthol-ammonia clusters, assumes a continuum of product states [11]. A free proton product potential, as assumed by HBKB, is plotted in Fig. 4. In this picture reactivity is not governed by solvent dynamics. The important parameters affecting the tunneling rate constant can be compared for these two models by the following expressions

$$k = \nu_1 \exp[-2\Omega] \quad \text{(bound-free transition)} \tag{1}$$

$$k = \frac{h\nu_1^2}{2\pi} \exp[-2\Omega] \left(\frac{\pi\beta}{\lambda_S}\right)^{1/2} \exp[-\beta\Delta G^{\ddagger}] \quad \text{(bound-bound transition)} \tag{2}$$

where ν_1 is the O—H vibrational frequency and

$$\Omega = \frac{\pi^2 a}{h} (2mU)^{1/2} \tag{3a}$$

$$\Delta G^{\ddagger} = (\lambda_S + \Delta G_0)^2 / 4\lambda_S \tag{3b}$$

$$\beta = (k_b T + E_{\text{vib}}/s)^{-1}. \tag{3c}$$

The terms in Ω and $\Delta G^{\ddagger}$ are defined in Figs. 4 and 5. T is the initial cluster temperature (k_b is the Boltzmann constant), E_{vib} is the vibrational excitation energy in S_1, and s is the number of effective degrees of freedom in the cluster that contribute to the heat capacity.

We present these equations not to draw quantitative conclusions, but to show what parameters and properties are important in tunneling and, therefore, worthy of measuring. The tunneling models are discussed in greater

depth elsewhere [32]. For example (1)–(3) are integrated over the O···N vibrational wavefunctions in order to include the important effect of barrier modulation. Here, we are simply interested in measuring the rate of solvent reorganization k_s and the magnitude of the solvent-solute interaction, λ_S by TR/PES.

4.2. *Solvent reorganization energy*

When proton transfer occurs, the solvent is no longer at equilibrium. The formation of a large product dipole is expected to exert a force on the solvent leading to further dynamics. For simplicity, we consider that reaction and solvent dynamics are separable, that is

$$\mathrm{PhOH^*}\cdots B_n \xrightarrow[k]{} [\mathrm{PhO^{*-}}\cdots \mathrm{H^+}\, B_n]_{ur}$$

$$\xrightarrow[k_s]{} [\mathrm{PhO^{*-}}\cdots \mathrm{H^+}\, B_n]_r$$

where the subscripts *ur* and *r* denote unrelaxed and relaxed solvent configurations and k_s is the solvent reorganization rate constant (cf. Fig. 2). The product formation curves we recorded show two time-dependences of comparable amplitude, a rapid rise matching the decay of the $\mathrm{PhOH^+(NH_3)_n}$ signals (55–70 ps) and a much slower growth component of about 300 ps [2]. The fast time respone is due to the ESPT reaction. The slow time response is ascribed to solvent cluster reorganization.

How the potential energy along the O—H coordinate might change with time due to solvent reorganization is illustrated qualitatively in Fig. 2. The solvent network reorganizes to achieve a structure that best accomodates the proton (and counterion). This reorganization or "solvation of the proton" causes delocalization of charge and lengthening of the O—H bond. The relaxing ion-pair moves closer to a geometry representing the cluster-ion equilibrium configuration. This improves the Franck-Condon (FC) factors for ionization and leads to an increased ionization efficiency with time. The details of this simple kinetic model are given elsewhere [2, 6].

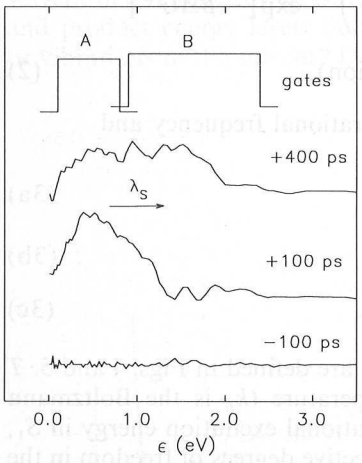

Fig. 6. Time-resolved photoelectron spectra as a function of pump-probe delay time *t*. These are difference spectra corresponding to $(\lambda_1+\lambda_2)-(\lambda_1)$. Electrons were accelerated by an additional 2 eV to increase detection efficiency of low-energy electrons. Constant gate widths of 140 ns appear as different widths on the linear energy scale

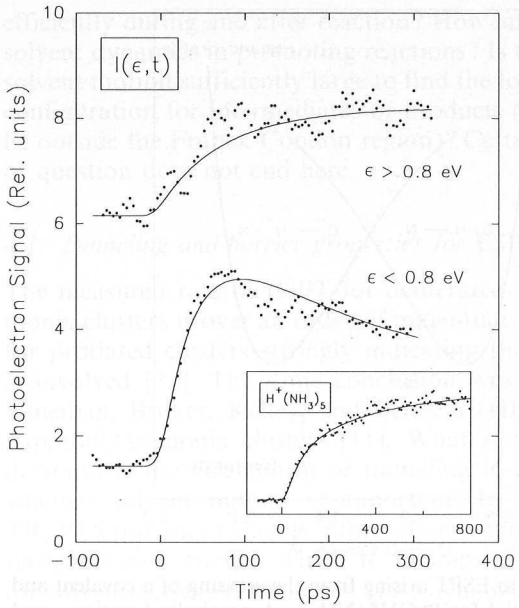

Fig. 7. Time-dependence of low-energy ($0 < \varepsilon < 0.8$ eV) and high-energy ($0.8 < \varepsilon < 2.6$ eV) photoelectron bands (using 140-ns gates under conditions of Fig. 2a). *Fitted curves* were calculated for rate constants $k = (50\ \mathrm{ps})^{-1}$ and $k_s = (300\ \mathrm{ps})^{-1}$ and spectral parameters $\varepsilon_0 = 0.7$ eV, $\sigma = 0.6$ eV, and $\lambda_S = 0.5$ eV. Calculated decay and formation curves correspond to $\varepsilon = 0.5$ eV and 1.2 eV, respectively. *Insert* shows time dependence for total product ion yield fitted to values of $k = (65\ \mathrm{ps})^{-1}$ and $k_s = (300\ \mathrm{ps})^{-1}$ [6]

A more definitive measure of geometry change is to monitor individual FC components to ionization. This is achieved by time-resolved photoelectron spectroscopy [6]. In Fig. 6 photo-electron spectra are plotted for different probe delay times. The spectra are broad because of the distribution of cluster sizes, large density of low-frequency modes, rapid vibrational redistribution, and large geometry change upon ionization. The $t = -100$ ps spectrum is identical to the 266-nm only spectrum (not shown), which arises from ionization of smaller unreactive cluster sizes to form the $\mathrm{PhOH^+(NH_3)_n}$ complex (Fig. 2). The energy-resolved spectra in Fig. 6 were obtained by subtracting the strong 266-nm only signal. (The subtraction was not applied to the time-resolved traces in Fig. 7, therefore, the baseline levels contain a contribution from the constant 266-nm only signal.) For positive *t*, a low-energy photoelectron band appears. Low-energy electrons correspond to high-internal-energy ions and would be the outcome of poor FC factors to ionization. However, in time, the solvent reorganizes to better solvate the proton and evolves to a geometry that is more similar to the ion geometry. As a result, the FC factors for ionization improve (become more vertical) leading to lower internal-energy ions (i.e., higher energy electrons). This is observable in the photoelectron spectra by a band that shifts to increasing energy with time, and is analogous to the method of time-dependent Stokes shifts to emission bands used to measure solvent relaxation in the condensed phase [37–40]. The magnitude of the spectral shift is related to the solvent reorganization energy λ_S.

4.3. Time dependence of the photoelectron bands

Time-dependent spectral shifts in emission bands have been used to measure solvent relaxation in condensed phase. In these experiments, the relaxation dynamics are generally related by the correlation function

$$C(t)=\frac{\nu(t)-\nu(\infty)}{\nu(0)-\nu(\infty)} \tag{4}$$

where $\nu(t)$, $\nu(0)$, and $\nu(\infty)$ are the emission maxima at time t, $t=0$, and $t=\infty$, respectively [37–40]. $C(t)$ is predicted to decay exponentially in a pure Debye solvent with a longitudinal relaxation time constant τ_L. It is reasonable to expect that time-dependent photoelectron spectroscopy should be sensitive to similar structural dynamics in clusters.

We apply a simple model for describing the time dependence of the photoelectron spectrum by assuming that the Franck-Condon photoelectron band is a Gaussian of width σ and shifts by λ_S due to solvent reorganization [6, 40]. These assumptions are not rigorous. Although, the spectral shift is a function of λ_S, the actual dependence is difficult to know without knowledge of the shapes of the potential surfaces for the initial and final states involved in the photoelectron transition. Also, some solvent rearrangement might already have occurred in the reactant in order to achieve the critical configuration for reaction. In this case the energy change due to the remaining solvent rearrangement in the product could be less than that nominally defined by λ_S. The simple model presented here to describe the observed photoelectron spectral shifts and time-dependence is only a first step toward understanding the details of solvent rearrangement.

The time dependence as a function of photoelectron energy ε is given by

$$g(\varepsilon,t)=\exp\left\{-\frac{[(\varepsilon_0+\lambda_S-\varepsilon)-\lambda_S\rho(t)]^2}{\sigma^2}\right\} \tag{5}$$

where ε_0 is the energy of the band maximum at $t=0$ (unrelaxed spectrum) and $\rho(t)$ is the time dependence for the band maximum. The function $\rho(t)$, which is equivalent to $C(t)$ in (4) in this simple model, is a measure of cluster relaxation along the solvent coordinate. We define $\rho(t)$ as a decaying function [$\exp(-k_s t)$ hereafter] so that the band maximum $\varepsilon_0+\lambda_S[1-\rho(t)]$ is ε_0 at $t=0$ and $\varepsilon_0+\lambda_S$ at $t=\infty$. For positive λ_S, the photoelectron band shifts to higher energy (i.e., lower ion energy), corresponding to a redshift in terms of the product-state to ion-state transition energy. This is the predicted direction of change for a solvent cluster that undergoes a change in configuration that better resembles the equilibrium geometry of the cluster ion. Some of the assumptions of our simple model include describing the solvent modes classically by a single reorganization parameter λ_S, ignoring internal modes in the Franck-Condon distribution, assuming a constant width parameter σ with time, and assuming a constant integrated photoelectron band intensity with time.

To illustrate the expected time dependence as a function of photoelectron energy, we consider the simple case of $\varepsilon=\varepsilon_0$ and $\varepsilon=\varepsilon_0+\lambda_S=\varepsilon_\infty$. This represents the intensity at the peak positions for $t=0$ and $t=\infty$. From (5), we obtain

$$g(\varepsilon_0,t)=\exp\left\{-\frac{\lambda_S^2}{\sigma^2}(1-e^{-k_s t})^2\right\} \tag{6a}$$

$$g(\varepsilon_\infty,t)=\exp\left\{-\frac{\lambda_S^2}{\sigma^2}e^{-2k_s t}\right\}. \tag{6b}$$

These expressions show that $g(\varepsilon_0,t)$ decreases with time and $g(\varepsilon_\infty,t)$ increases with time. It is easy to see that at the asymptotic limits $t=0$ and $t=\infty$, the intensity approaches a plateau level. The function $g(\varepsilon,t)$ is sensitive to the values of ε, the spectral parameters λ_S and σ, and the functional form of $\rho(t)$. Accurate determination of each of these properties can be obtained by recording a series of time-resolved measurements over narrow electron energy bands or by recording the evolving photoelectron band over narrow time intervals.

The observed time dependences in Fig. 7 were fitted by the expression

$$I(\varepsilon,t)=\int_{-\infty}^{\infty} f(t-t')[1-e^{-kt'}]g(\varepsilon,t')\,\mathrm{d}t' \tag{7}$$

which includes the instrument time response and ESPT product formation kinetics. Because the timescale for these functions is much shorter than for solvent reorganization, the time dependence for the observed signal $I(\varepsilon,t)$ is nearly equivalent to $g(\varepsilon,t)$.

The time dependence for the low-energy and high-energy photoeletron bands (gates A and B) is plotted in Fig. 7. The low-energy band (high-energy ions) increases rapidly in intensity and then decays at a slower rate. The high-energy band (low-energy ions) shows a corresponding slow rate of increase. These observations support the interpretation of a Franck-Condon distribution that changes with time due to solvent reorganization. The calculated curves in Fig. 7 are based on the above model [6]. At this preliminary stage of analysis, the fits are not quantitative; however, the rate constants $k=(50\text{ ps})^{-1}$ and $k_s=(300\text{ ps})^{-1}$, used to fit the data, are in good agreement with the time-resolved mass spectrometry results.

The measured rate constants k and k_s can be interpreted in context of condensed-phase solvation. It is generally assumed that electron transfer (ET) and proton transfer (PT) tunneling rates are limited by solvent relaxation such that $k\leqq\tau_L^{-1}$ (i.e., dynamic solvent effect; $k\sim\tau_L^{-1}$ for barrierless process). In hydrogen-bonding solvents it is common to refer to three Debye (dielectric response) relaxation times due to large amplitude aggregate motions involving hydrogen-bonding dynamics (τ_{D1}), molecular rotation or reorientation (τ_{D2}), and internal rotation (τ_{D3}, more relevant to alcohols than to NH_3) [37–40]. The lowest frequency motions are known to dominate the dielectric response of a solvent and hence τ_{D1} is usually associated with τ_L. Simple theories then

predict that the rates of ET and PT should not exceed τ_L^{-1}. Our results, however, show that the rate constant k for ESPT is substantially faster than k_s in these clusters. Similar rate disparities have been observed in the condensed phase [37–40], and recent theories now cite the importance of higher frequency solvent fluctuations and solute intramolecular modes to chemical rates [41]. A plausible interpretation of our cluster dynamics is that ESPT is facilitated by reorientational solvent fluctuations ($k \sim \tau_{D2}^{-1}$) or intramolecular solute dynamics and that k_s, which measures geometry changes, is associated with τ_{D1}.

Needless to say, the above interpretation is tentative and somewhat speculative. Hopefully, these results will point the way for additional experiments and calculations. It would be helpful in the latter regard to have some estimates of the potential energies along the relevant coordinates to reaction.

5. Correspondence to bimolecular gas-phase reactions

In this section we describe an application of PES of clusters to the study of gas-phase properties of bimolecular reactions. van der Waals (vdW) complexes are a useful way to study the bound and quasibound reactive complexes associated with gas-phase bimolecular collisions [42, 43]. Ionization of vdW complexes to form reactive complexes of ion-molecule reactions [44–49] is especially favorable because they tend to be stable due to charge-induced dipole interactions, in contrast to neutral-neutral complexes which are often unbound and associated with a saddle-point region on a potential energy surface.

Ion-molecule kineticists, for many years, have postulated that some reactions (mostly fast) proceed along barrierless single-well reaction coordinates whereas other reactions (mostly slow) involve double-well barrier processes [50]. Included in the latter group were classes of reactions in which the charge distribution in the reactant was delocalized from the eventual charged leaving group. The double-minima barrier mechanism [50, 51] became widely accepted well before the existence of two distinct and stable reactive complexes was experimentally confirmed [3]. The difference between a single-well and double-well reaction coordinate for the gas-phase proton transfer reaction

$$PhOH^+ + NH_3 \rightarrow PhO + NH_4^+$$

is illustrated in Fig. 8. Because $PhOH^+$ has a ground electronic-state charge distribution delocalized from the potential proton leaving group, we decided to investigate the possibility of detecting two stable complex forms with NH_3.

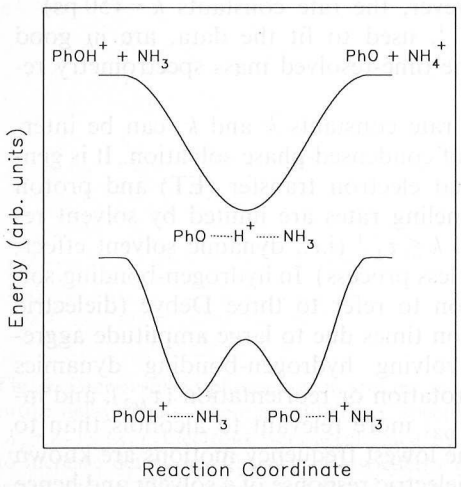

Fig. 8. Representation of single- and double-well reaction coordinates for the reaction $PhOH^+ + NH_3 \rightarrow PhO + NH_4^+$

5.1. *Detection and elucidation of barrier properties*

The energy diagram in Fig. 2 implies that there are two stable complexes for $PhOH^+(NH_3)_n$. We explain shortly how the energy diagram was derived. First, we present the experimental evidence for the double-minima reaction mechanism. Because of the known chemistry of ESPT described early, it is possible to ionize to the inner well or the outer well of the cluster ion potential curve by choosing either prompt ionization or delayed ionization, respectively, following photoexcitation to PhOH* (Fig. 2). This picosecond delayed-ionization technique was essential for probing the two possible complexes $PhOH^+ \cdots B_n$ and $PhO \cdots H^+ B_n$. The mass spectra obtained by selectively ionizing to the inner and outer cluster ion wells are given in Fig. 9. For prompt ionization using one-color, two-photon ionization at 266 nm, one observes mostly parent ion $PhOH^+(NH_3)_n$ with very little evidence of dissociation to $PhO + H^+(NH_3)_n$ (Fig. 9a). The photoexcitation energy exceeds the ionization potential by greater than 2 eV for $n \geqq 4$ suggesting that a significant barrier exists for the exothermic proton transfer reaction. Dissociation was observed by surmounting the barrier by the absorption of a third photon, which was achieved by increasing the laser pulse energy (Figs. 9b, c).

Other evidence of a large barrier to proton transfer for $PhOH^+ \cdots NH_3$ was reported by Mikami and coworkers [44]. Their experiment used nanosecond two-color resonance threshold ionization to measure the ionization potential of the complex $PhOH \cdot NH_3$ (7.71 eV) and the appearance potential for producing $PhOH^+ + NH_3$ (8.72 eV) [44]. No NH_4^+ was observed implying that proton transfer is either impeded by a large barrier or forms a very stable product complex $PhO \cdots H^+ NH_3$ that does not readily dissociate. Our delayed-ionization mass spectra in Figs. 9d, e, however, show that dissociation is very facile on the product side of the barrier. These measurements were made using either 355-nm or 532-nm ionization (the latter wavelength is a two-photon ionization). It should be noted that the outer-well complex is only accessible to cluster sizes that undergo ESPT, namely $n > 4$ (cf. Fig. 3b). The appearance of product signal $H^+(NH_3)_n$ for $n \leqq 4$ occurs from $n > 4$ cluster ions that evaporate following proton transfer due to the excess ionization energy and reaction exothermicity.

We discuss two remaining questions of interest: (1) is the product complex $PhO \cdots H^+(NH_3)_n$ bound or dissociative and (2) what is the barrier height? The former

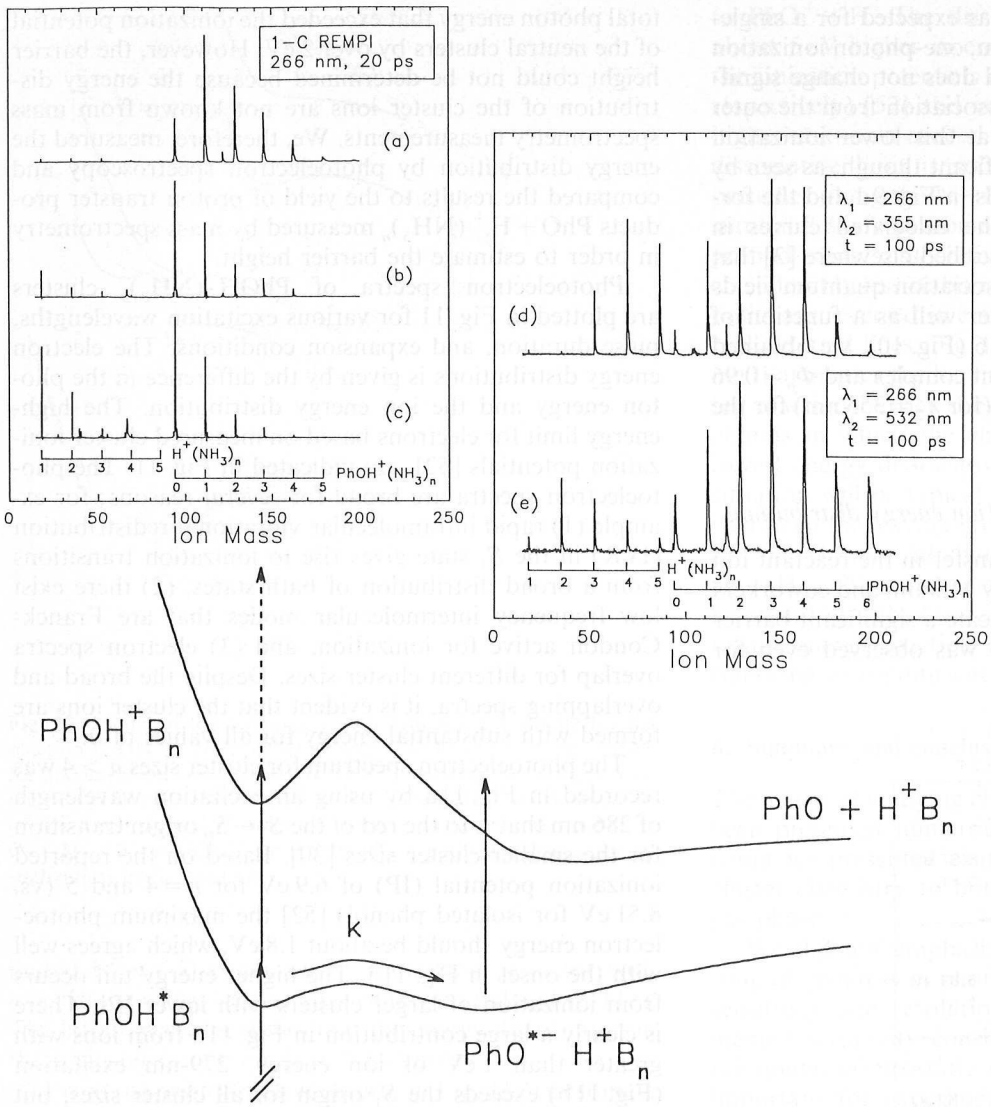

Fig. 9. Picosecond REMPI mass spectra: *(a–c)* One-color excitation with 20-ps, 266-nm pulses of increasing energy. *(a)* two-photon excitation, *(b)* appearance of $H^+(NH_3)_n$ by three-photon excitation, *(c)* increased three-photon signal and appearance of aromatic fragments at the four-photon level *(d–e)*. Two-color delayed ionization to the outer ion well. *(d)* $\lambda_2 = 355$-nm, one-photon ionization, and *(e)* $\lambda_2 = 532$-nm, two-photon ionization

question was solved using picosecond pump-probe measurements and the latter using the combined evidence of photo-electron spectroscopy and photofragment mass spectrometry. These are described below.

5.2. *A bound product complex*

We used time-resolved measurements to establish that the products $H^+(NH_3)_n$ observed in Figs. 9d, e occur by dissociation from the outer potential well and not the inner well. Measurements of PhOH* $(NH_3)_n$ reactant decay [by detecting $PhOH^+(NH_3)_n$] and $PhO^{*-}H^+(NH_3)_n$ product formation [by detecting $H^+(NH_3)_n$] are shown in Fig. 10. The $PhOH^+(NH_3)_n$ signal decays to the baseline when using 532-nm, two-photon ionization (Fig. 10a), indicating that ionization to the outer well is almost completely dissociative. The growth rate of the $H^+(NH_3)_n$ product signal matches the decay rate of the

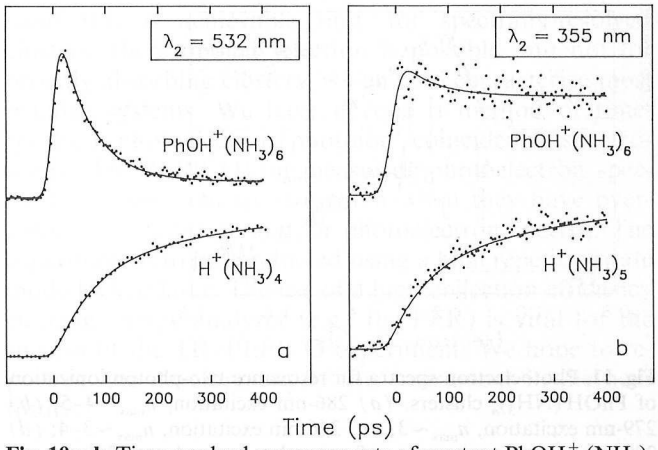

Fig. 10a, b. Time-resolved measurements of reactant $PhOH^+(NH_3)_n$ and product $H^+(NH_3)_n$ signals for cluster size $n=6$. **a** $\lambda_2 = 532$-nm, two-photon ionization, **b** $\lambda_2 = 355$-nm, one-photon ionization. We show $H^+(NH_3)_4$ traces for $n=4$ and $n=5$ because, typically, two and one solvent molecules evaporate at these respective ionization energies. The model used to calculate curves is described elsewhere [3]

$PhOH^+(NH_3)_n$ reactant signal as expected for a single-step reaction. When using 355-nm, one-photon ionization (Fig. 10b), the reactant ion yield does not change significantly with t, indicating that dissociation from the outer potential well is less extensive at this lower ionization energy. Dissociation is still significant though, as seen by the prominent $H^+(NH_3)_n$ signals in Fig. 9d and the formation kinetics in Fig. 10b. The calculated curves in Fig. 10 are based on a model described elsewhere [3] that enables one to determine the dissociation quantum yields Φ from both the inner and outer well as a function of cluster size. For cluster size $n=6$ (Fig. 10), we obtained values of $\Phi_r \leqq 0.10$ for the reactant complex and $\Phi_p = 0.96$ (for $\lambda_2 = 532$ nm) and $\Phi_p = 0.65$ (for $\lambda_2 = 355$ nm) for the product complex.

5.3. *Photoelectron spectroscopy/ion energy distributions*

The measurements of proton transfer in the reactant ion complexes $PhOH^+\cdots(NH_3)_n$ by Mikami and coworkers [44] and by our group [3, 5] indicate a significant barrier to reaction. Very little reaction was observed even for total photon energy that exceeded the ionization potential of the neutral clusters by over 2 eV. However, the barrier height could not be determined because the energy distribution of the cluster ions are not known from mass spectrometry measurements. We, therefore, measured the energy distribution by photoelectron spectroscopy and compared the results to the yield of proton transfer products $PhO + H^+(NH_3)_n$ measured by mass spectrometry in order to estimate the barrier height.

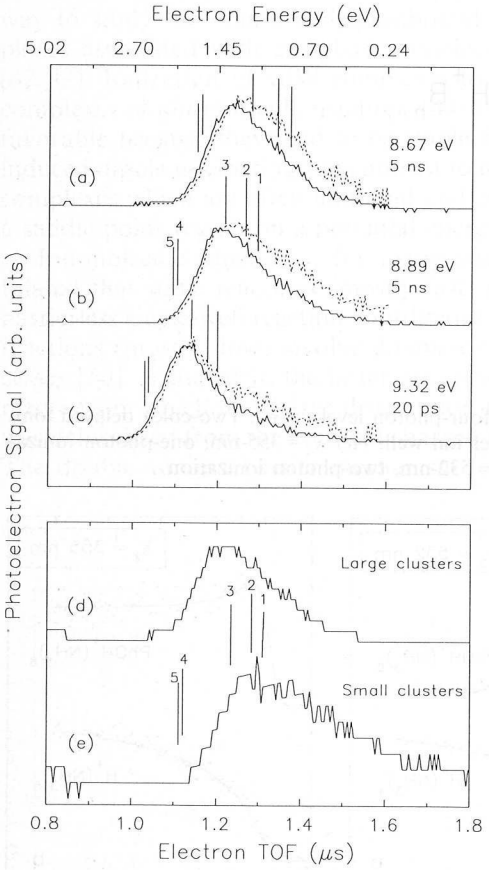

Fig. 11. Photoelectron spectra for resonance two-photon ionization of $PhOH(NH_3)_n$ clusters. *(a)* 286-nm excitation, $n_{max} \sim 4$–5; *(b)* 279-nm excitation, $n_{max} \sim 3$; *(c)* 266-nm excitation, $n_{max} \sim 3$–4; *(d)* 280-nm excitation at center of gas pulse, $n_{max} \sim 4$; *(e)* 280-nm excitation at edge of gas pulse, $n_{max} \sim 2$. The n_{max} values are estimated from mass spectra and knowledge of cluster $S_0 \rightarrow S_1$ transition energies. The *vertical lines* represent IPs for clusters of size n. The *dotted curves* in *(a)–(c)* are corrected for electron kinetic energy detection efficiency

Photoelectron spectra of $PhOH\cdot(NH_3)_n$ clusters are plotted in Fig. 11 for various excitation wavelengths, pulse duration, and expansion conditions. The electron energy distributions is given by the difference in the photon energy and the ion energy distribution. The high-energy limit for electrons based on measured cluster ionization potentials [52], are indicated in Fig. 11. The photoelectron spectra are broad for several reasons; for example (1) rapid intramolecular vibrational redistribution (IVR) in the S_1 state gives rise to ionization transitions from a broad distribution of bath states, (2) there exist low frequency intermolecular modes that are Franck-Condon active for ionization, and (3) electron spectra overlap for different cluster sizes. Despite the broad and overlapping spectra, it is evident that the cluster ions are formed with substantial energy for all values of n.

The photoelectron spectrum for cluster sizes $n > 4$ was recorded in Fig. 11a by using an excitation wavelength of 286 nm that is to the red of the $S_1 \leftarrow S_0$ origin transition for the smaller cluster sizes [30]. Based on the reported ionization potential (IP) of 6.9 eV for $n=4$ and 5 (vs. 8.51 eV for isolated phenol) [52] the maximum photoelectron energy should be about 1.8 eV, which agrees well with the onset in Fig. 11a. The higher energy tail occurs from ionization of larger clusters with lower IPs. There is clearly a large contribution in Fig. 11a from ions with greater than 1 eV of ion energy. 279-nm excitation (Fig. 11b) exceeds the S_1 origin for all cluster sizes, but is only resonant for $n > 2$, because of their broad absorption spectra [30, 44] (the mass spectrum peaks at $n=3$). The photoelectron energies corresponding to the cluster ion thresholds for $n=3$ and 4 are 1.38 and 2.0 eV, respectively. Again the ion energy distribution extends to relatively high energy.

The photoelectron spectra in Fig. 11 are due primarily to ionization of the complex $PhOH^+\cdots(NH_3)_n$ and not $PhO\cdots H^+(NH_3)_n$. The latter complex is produced if the intermediate S_1 state undergoes excited-state proton transfer (ESPT) before ionization. As discussed earlier, this occurs in about 60 ps for $n \geqq 5$ at 2500 cm^{-1} above the S_1 origin [2]. To avoid the possibility of ESPT, we recorded the spectrum in Fig. 11c using prompt (20-ps 266-nm) excitation/ionization. The photoelectron energies for the ion origins of $n=3$ and 4 are 1.81 and 2.43 eV, respectively. The ion energy distribution is similar to the cases using longer-wavelength nanosecond excitation. The spectra in Figs. 11d and 11e demonstrate that the cluster ions for $n=1$ and 2 are also formed with substantial energy. These spectra compare the results for a large cluster distribution (but not greatly exceeding $n=6$) produced by ionization in the cold central portion of the gas pulse (Fig. 11d) and for a small cluster distribution (dom-

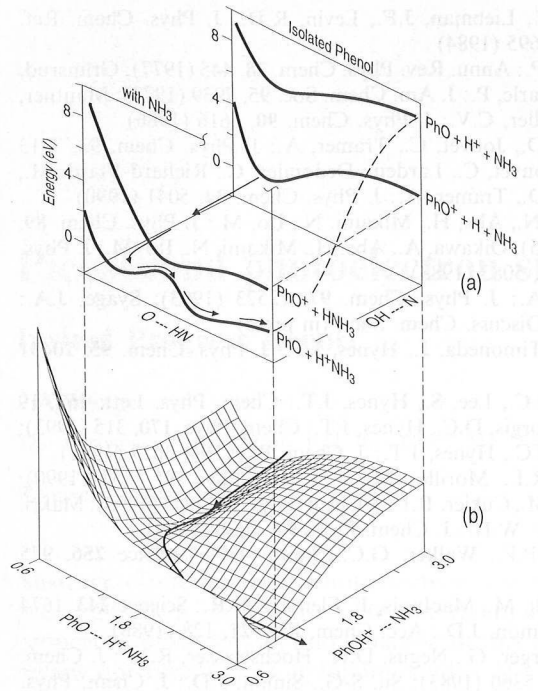

Fig. 12. Model of the potential energy reaction coordinate for the reaction $PhOH^+ + NH_3 \rightarrow PhO + NH_4^+$. *(a)* Potential energy curves for uncomplexed and complexed $PhOH^+$ showing the surface crossing that gives rise to the barrier to proton transfer. *(b)* A rendition of the lower adiabatic potential energy surface for the collinear O···H···N coordinate (in Å). Reaction paths are drawn for visualization in *(a)* and *(b)*

inated by $n \leqq 3$) produced by ionization resonant with $n = 1$ in the warm leading edge of the gas pulse (Fig. 11e). The latter spectrum shows that the energy distribution in these cluster ions extends to high energy.

From the photoelectron spectra in Fig. 11, we estimate that the fraction of cluster ions with greater than 1 eV of energy is at least 10% for all values of n considered here [5]. The mass spectrometry results presented earlier (cf. Fig. 9a) indicate that less than 10% of the complex ions dissociate to NH_4^+ [3, 44]. These complementary observations allow us to place a lower limit of about 1 eV on the proton-transfer barrier height. The predicted upper limit, based a surface crossing potential energy model [3, 5] summarized below, is about 1.5 eV.

5.4. Potential energy diagram and reaction coordinate

The model proposed for the potential energy surface and reaction coordinate is pictured in Fig. 12 [5]. Potential energy curves along the O—H coordinate are drawn for isolated $[PhOH]^+$ (back panel) and for $[PhOH \cdot NH_3]^+$ (front panel). The N—H coordinate running from back to front represents the approach of reactants in a bimolecular reaction and the O—H coordinate, just mentioned, represents departure of products. The reaction coordinate is approximated by the path marked by arrows.

The barrier is predicted on the basis of a simple concept. The ground electronic state of $PhOH^+$ dissociates to $PhO^+ + H$. The dissociative limit for $PhO + H^+$ is about 5 eV higher in energy (given by the difference in the ionization potentials of PhO and H, 8.56 and 13.60 eV, respectively) [52] and is probably associated with some higher unknown excited electronic state of $PhOH^+$. This dissociative limit is stabilized enormously as NH_3 approaches along the N—H coordinate because of the substantial 8.86 eV proton affinity [28] of NH_3. Because the ground state dissociative limit $PhO^+ + H$ experiences considerably less stabilization from NH_3, the dissociative limits are reversed in energy by the approach of reactant NH_3 (dotted lines, Fig. 12a). This causes a surface crossing that creates the barrier to reaction. The surface crossing reaction barrier should be a general property of reactions in which the charged leaving group is not the lowest energy dissociative limit of the isolated ion. This situation will be typical of ions where charge is delocalized from the leaving group. A visualization of the shape of the lower adiabatic surface for the collinear O···H···N coordinate, based on the model in [3], is given in Fig. 12b. The reaction path drawn represents the lowest energy reaction coordinate in the classical limit (ignoring zero-point energy).

6. Summary and conclusions

The merits of studying chemical reactions in clusters have been presented numerous times in the past. In this account we presented examples of the correspondence of cluster chemistry to both the condensed-phase and the gas-phase.

We did not emphasize experimental details and the state of progress in photoelectron spectroscopy. Greater sensitivity and resolution is always the goal. We augmented sensitivity considerably by incorporating a paraboloidal electrostatic reflector (PER). This feature is important for experiments that use low pulse energies (e.g., ultrafast lasers) and that have low sample density (e.g., clusters of a specific size). Another important capability for cluster studies is a means to record photoelectron spectra for specific cluster size. In our experiment this is achievable only for spectrally-resolved clusters where optical selection is possible, but not for broadly absorbing clusters, which tend characterize most reactive systems. We have devised a method of time-resolved photoelectron/photoion coincidence spectroscopy (TR/PEPICO) for measuring photoelectron spectra for specific cluster sizes even when they have overlapping excited-state and/or photoelectron spectra. The experiment is to be conducted using a high repetition rate mode-locked laser. The use of a high collection efficiency electron energy analyzer (e.g., the PER) is vital for the success of the TR/PEPICO experiment. We hope to report on the development of this instrument in the near future.

References

1. Syage, J.A., Steadman, J.: Chem. Phys. Lett. **166**, 159 (1990); Steadman, J., Fournier, E.W., Syage, J.A.: Appl. Opt. **29**, 4962 (1990)

2. Steadman, J., Syage, J.A.: J. Chem. Phys. **92**, 4630 (1990); Syage, J.A., Steadman, J.: J. Chem. Phys. **95**, 2497 (1991)
3. Steadman, J., Syage, J.A.: J. Am. Chem. Soc. **113**, 6786 (1991)
4. Steadman, J., Syage, J.A.: J. Phys. Chem. **95**, 10326 (1991)
5. Syage, J.A., Steadman, J.: J. Phys. Chem. **96**, 9606 (1992)
6. Syage, J.A.: Chem. Phys. Lett. **202**, 227 (1993)
7. Breen, J.J., Peng, L.W., Willberg, D.M., Heikal, A., Cong, P., Zewail, A.H.: J. Chem. Phys. **92**, 805 (1990)
8. Willberg, D.M., Gutmann, M., Breen, J.J., Zewail, A.H.: J. Chem. Phys. **96**, 198 (1992). Gutmann, M., Willberg, D.M., Zewail, A.H.: J. Phys. **97**, 8037, 8048 (1992)
9. Ray, D., Levinger, N.E., Papanikolas, J.M., Lineberger, W.C.: J. Chem. Phys. **91**, 6533 (1989); Papanikolas, J.M., Gord, J.R., Levinger, N.E., Ray, D., Vorsa, V., Lineberger, W.C.: J. Phys. Chem. **95**, 8028 (1991)
10. Cassasa, M.P., Stephenson, J.C., King, D.S.: J. Chem. Phys. **89**, 1966 (1988); Fuke, K., Keizo, K., Misaizu, F., Kaya, K.: J. Chem. Phys. **95**, 4074 (1991)
11. Hineman, M.F., Bruker, G.A., Kelley, D.F., Bernstein, E.R.: J. Chem. Phys. **97**, 3341 (1992)
12. Wei, S., Purnell, J., Buzza, S.A., Stanley, R.J., Castleman, Jr., A.W.: J. Chem. Phys. **97**, 9480 (1992); Wei, S., Purnell, J., Buzza, S.A., Castleman, Jr., A.W.: J. Chem. Phys. **99**, 755 (1993)
13. Steadman, J., Syage, J.A.: Rev. Sci. Instrum. **64**, 3094 (1993)
14. Kimura, K.: Adv. Chem. Phys. **60**, 161 (1985)
15. Smith, J.M., Lakshminarayan, C., Knee, J.L.: J. Chem. Phys. **93**, 4475 (1990)
16. Song, X., Wilkerson, C.W. Jr., Lucia, J., Pauls, S., Reilly, J.P.: Chem. Phys. Lett. **174**, 377 (1990)
17. Kimura, K., Sato, K., Okuyama, K., Takahashi, M.: In: Ultrafast Phenomena 6, p. 483, Yajima, T., Yoshihara, K., Harris, C.B., Shionoya, S. (eds.). Berlin, Heidelberg, New York: Springer 1988
18. Baumert, T., Röttgermann, C., Rothenfusser, C., Thalweiser, R., Weiss, V., Gerber, G.: Phys. Rev. Lett. **69**, 1512 (1992)
19. Kim, B., Thantu, N., Weber, P.M.: J. Chem. Phys. **97**, 5384 (1992)
20. Smith, J.M., Zhang, X., Knee, J.L.: J. Chem. Phys. **99**, 2550 (1993)
21. Trevor, D.J., Van Woerkom, L.D., Freeman, R.R.: Rev. Sci. Instrum. **60**, 1051 (1989)
22. Kruit, P., Read, F.H.: J. Phys. E**16**, 313 (1983)
23. Müller-Dethlefs, K., Schlag, E.W.: Ann. Rev. Phys. Chem. **42**, 109 (1991)
24. Cheshnovsky, O., Leutwyler, S.: Chem. Phys. Lett. **121**, 1 (1985); Cheshnovsky, O., Leutwyler, S.: J. Chem. Phys. **88**, 4127 (1988); Droz, T., Knochenmuss, R., Leutwyler, S.: J. Chem. Phys. **93**, 4520 (1990)
25. Kosower, E.M., Huppert, D.: Annu. Rev. Phys. Chem. **37**, 127 (1986)
26. Lee, J., Griffin, R.D., Robinson, G.W.: J. Chem. Phys. **82**, 4920 (1985); Lee, J., Robinson, G.W., Webb, S.P., Philips, L.A., Clark, J.H.: J. Am. Chem. Soc. **108**, 6538 (1986)
27. Huppert, D.H., Jayaraman, A., Maines, R.G. Sr., Steyert, D.W., Rentzepis, P.M.: J. Chem. Phys. **81**, 5596 (1984)
28. Lias, S.G., Liebman, J.F., Levin, R.D.: J. Phys. Chem. Ref. Data **13**, 695 (1984)
29. Kebarle, P.: Annu. Rev. Phys. Chem. **28**, 445 (1977); Grimsrud, E.P., Kebarle, P.: J. Am. Chem. Soc. **95**, 7939 (1973); Mautner, M.J., Speller, C.V.: J. Phys. Chem. **90**, 6616 (1986)
30. Solgadi, D., Jouvet, C., Tramer, A.: J. Phys. Chem. **92**, 3313 (1988); Jouvet, C., Lardeux-Dedonder, C., Richard-Viard, M., Solgadi, D., Tramer, A.: J. Phys. Chem. **94**, 5041 (1990)
31. Gonohe, N., Abe, H., Mikami, N., Ito, M.: J. Phys. Chem. **89**, 3642 (1985); Oikawa, A., Abe, H., Mikami, N., Ito, M.: J. Phys. Chem. **87**, 5083 (1983)
32. Syage, J.A.: J. Phys. Chem. **97**, 12523 (1993); Syage, J.A.: Faraday Discuss. Chem. Soc.: (in press)
33. Juanós i Timoneda, J., Hynes, J.T.: J. Phys. Chem. **95**, 10431 (1991)
34. Borgis, D.C., Lee, S., Hynes, J.T.: Chem. Phys. Lett. **162**, 19 (1989); Borgis, D.C., Hynes, J.T.: Chem. Phys. **170**, 315 (1993); Borgis, D.C., Hynes, J.T.: J. Chem. Phys. **94**, 3619 (1991)
35. Cukier, R.I., Morillo, M.: J. Chem. Phys. **91**, 857 (1990); Morillo, M., Cukier, R.I.: J. Chem. Phys. **92**, 4833 (1990); Makri, N., Miller, W.H.: J. Chem. Phys. **91**, 4026 (1989)
36. Barbara, P.F., Walker, G.C., Smith, T.P.: Science **256**, 975 (1992)
37. Maroncelli, M., MacInnis, J., Fleming, G.R.: Science **243**, 1674 (1989); Simon, J.D.: Acc. Chem. Res. **21**, 128 (1988)
38. Rothenberger, G., Negus, D.K., Hochstrasser, R.M.: J. Chem. Phys. **79**, 5360 (1983); Su, S-G., Simon, J.D.: J. Chem. Phys. **89**, 908 (1988)
39. Jarzeba, W., Walker, G.C., Johnson, A.E., Kahlow, M.A., Barbara, P.F.: J. Phys. Chem. **92**, 7039 (1988)
40. Kozik, M., Sutin, N., Winkler, J.R.: Coord. Chem. Rev. **97**, 23 (1990)
41. Hynes, J.T.: J. Phys. Chem. **90**, 3701 (1986); Sumi, H., Marcus, R.: J. Chem. Phys. **84**, 4894 (1986)
42. Wittig, C., Sharpe, S., Beaudet, R.A.: Acc. Chem. Res. **21**, 341 (1988); Radhakrishnan, G., Buelow, S., Wittig, C.: J. Chem. Phys. **84**, 727 (1986)
43. Halberstadt, N., Soep, B.: J. Chem. Phys. **80**, 2340 (1984)
44. Mikami, N., Okabe, A., Suzuki, I.: J. Chem. **92**, 1858 (1988)
45. Li, S., Bernstein, E.R.: J. Chem. Phys. **97**, 792, 804 (1992)
46. Brutschy, D., Janes, D., Eggert, J.: Ber. Bunsenges., Phys. Chem. **92**, 74 (1988)
47. Breen, J.J., Tzeng, W.-B., Kilgore, K., Keesee, R.G., Castleman Jr., A.W.: J. Chem. Phys. **90**, 19 (1989)
48. Syage, J.A.: J. Phys. Chem. **93**, 107 (1989)
49. Syage, J.A.: J. Chem. Phys. **92**, 1804 (1990)
50. Moylan, C.R., Brauman, J.I.: Ann. Rev. Phys. Chem. **34**, 187 (1983). Comita, P.B., Brauman, J.I.: Science **227**, 863 (1985). Gas Phase Ion Chemistry, Vols. I and II; Bowers, M.T. (ed.). New York: Academic Press 1979
51. Farneth, W.E., Brauman, J.I.: J. Am. Chem. Soc. **98**, 7891 (1976); Jasinski, J.M., Brauman, J.I.: J. Am. Chem. Soc. **102**, 2906 (1980)
52. Lias, S.G., Bartmess, J.E., Liebman, J.F., Holmes, J.L., Levin, R.D., Mallard, W.G.: J. Phys. Chem. Ref. Data: **17**, 1 (1988)